



# Unveiling anion induced surface reconstruction of perovskite oxide for efficient water oxidation

Jing Zhang<sup>a</sup>, Yu Ye<sup>a,b</sup>, Bo Wei<sup>c</sup>, Feng Hu<sup>a</sup>, Longtao Sui<sup>a</sup>, Huangwei Xiao<sup>a</sup>, Liangqi Gui<sup>a,d</sup>, Jian Sun<sup>a</sup>, Beibei He<sup>a,e,f,\*</sup>, Ling Zhao<sup>a,e,f,\*</sup>

<sup>a</sup> Faculty of Materials Science and Chemistry, China University of Geosciences, Wuhan 430074, China

<sup>b</sup> State Key Laboratory of Geological Processes and Mineral Resources, China University of Geosciences, Wuhan 430074, China

<sup>c</sup> School of Physics, Harbin Institute of Technology, 92 West Dazhi Str., Harbin 150001, China

<sup>d</sup> School of Physical and Mathematical Sciences, Nanyang Technological University, 21 Nanyang Link, 637371, Singapore

<sup>e</sup> Shenzhen Research Institute, China University of Geosciences, Shenzhen 518000, China

<sup>f</sup> Zhejiang Institute, China University of Geosciences (Wuhan), Hangzhou 311305, China

## ARTICLE INFO

### Keywords:

Perovskite oxide  
Dynamic surface reconstruction  
Anion regulation  
Operando Raman  
Oxygen evolution

## ABSTRACT

Perovskite oxides are a promising family of oxygen evolution reaction (OER) electrocatalysts. However, rational design of surface reconstruction on perovskite oxides to achieve high intrinsic activity is still a daunting challenge. Here, we demonstrate a facile anion defect approach to activate the surface reconstruction of perovskite oxide for OER. Experimental and theoretical investigations reveal that fluorine incorporation into  $\text{LaNi}_{0.75}\text{Fe}_{0.25}\text{O}_3$  (LNFO) perovskite with low vacancy formation energy facilitates surface transformation kinetics, creating electrochemically active oxyhydroxide layer. The reconstruction induced oxyhydroxide-perovskite heterostructure, in turn, enables a reduced energy barrier of OER relative to the pristine perovskite. As a demo, the optimized fluorine incorporated LNFO electrocatalyst exhibits an excellent OER performance with a low overpotential of 292 mV at 10  $\text{mA cm}^{-2}$ , significantly superior to the pristine LNFO and the benchmark  $\text{IrO}_2$  electrocatalysts. This finding offers new insights into activating surface reconstruction on perovskite oxide by engineering anion defect for water oxidation.

## 1. Introduction

The global goal of carbon neutral has encouraged people to pursue sustainable energy storage and conversion technologies. Large-scale water electrolysis is widely received as a next generation hydrogen and oxygen production system [1–4]. To advance this technology to commercialization, a core problem is promoting sluggish kinetics of oxygen evolution reaction (OER) because of its complicated four electron-proton transfer process, which prominently restricts the energy efficiency of the overall water splitting system [5–8].  $\text{IrO}_2$  and  $\text{RuO}_2$  are currently available OER electrocatalysts, but their extremely rarity, prohibitive cost and insufficient durability heavily hinder large-scale application in diverse renewable energy technologies [9]. This triggers the pursuit of precious metal-free OER electrocatalysts with high activity and long lifetime.

To this end, ever-rising interests have been attracted in perovskite oxides ( $\text{ABO}_3$ ) as alternative OER electrocatalysts owing to the

tunability of chemical composition and electronic structure, e.g.  $\text{Ba}_{0.5}\text{Sr}_{0.5}\text{Co}_{0.8}\text{Fe}_{0.2}\text{O}_{3-\delta}$  (BSCF) [10], and  $\text{PrBa}_{0.5}\text{Sr}_{0.5}\text{Co}_{1.5}\text{Fe}_{0.5}\text{O}_{5+\delta}$  (PBSCF) [11] etc. In typical perovskite structure, transition metal cation occupying in B-site is coordinated with oxygen anions as a formation of  $[\text{BO}_6]$  octahedra. These octahedras are corner/edge/face-shared with other adjacent octahedras to construct a three-dimension ordered framework. Several inner descriptors of perovskites involved in OER activity have been disclosed, including electron orbital occupancy [10], metal-oxygen interaction [12–14], oxygen vacancy density, [15,16] lattice-oxygen participation [17–20], etc. For example, Sr doped into  $\text{La}_{1-x}\text{Sr}_x\text{NiO}_3$  perovskite strengthened the hybridization between Ni and O, resulting in the accelerated charge transfer kinetics towards OER [21]. Fe substitution in  $\text{LaFe}_x\text{Ni}_{1-x}\text{O}_3$  perovskite with optimized electronic configuration and enhanced transition metal M 3d-O 2p hybridization contributed to a dramatically enhanced OER activity [22,23].

Despite these significant advances, perovskite oxides readily suffer from surface reconstruction issue under OER operating conditions,

\* Corresponding authors at: Faculty of Materials Science and Chemistry, China University of Geosciences, Wuhan 430074, China.

E-mail addresses: [babyfly@mail.ustc.edu.cn](mailto:babyfly@mail.ustc.edu.cn) (B. He), [zhaoling@cug.edu.cn](mailto:zhaoling@cug.edu.cn) (L. Zhao).

<https://doi.org/10.1016/j.apcatb.2023.122661>

Received 11 January 2023; Received in revised form 2 March 2023; Accepted 17 March 2023

Available online 20 March 2023

0926-3373/© 2023 Elsevier B.V. All rights reserved.

which in turn complicates the identification of electrochemical active sites [24–31]. Therefore, it is of a great implication to understand the underlying mechanism of surface structural transformation and the real active sites of perovskite oxides towards OER. As revealed,  $\text{Ba}^{2+}/\text{Sr}^{2+}$  could leach out from BSCF during OER operation, creating Co/Fe spinel-like surface. Such surface further dictated the surface reconstruction of electrochemically active Co(Fe)OOH, leading to an exceptional intrinsic activity of OER [24]. Compared to kinetically stable La termination  $\text{LaNiO}_3$  (LNO), Ni termination LNO conducted the surface reorganization with high OER performance [25]. Ce doping in A-site of  $\text{La}_{1-x}\text{Ce}_x\text{NiO}_3$  reduced the reconstruction potential to yield active NiOOH phase [26].  $\text{BaO}$  and  $\text{BaO}_2$  segregated on  $\text{Ba}_x\text{Sr}_{1-x}\text{Co}_{0.8}\text{Fe}_{0.2}\text{O}_{3-\delta}$  surface significantly benefited oxygen activation kinetics, ultimately boosting OER electrocatalysis [27].

Besides, it is well documented that engineering anion defect in electrocatalysts is another effortless and effective strategy to regulate their surface reconstruction behavior. For instance, a F doped NiFe hydroxide (NiFe-OH-F) nanosheet induced surface self-reconstruction, delivering an efficient OER activity [32]. Similar surface structural transformation has also been revealed in Cl incorporated  $\text{LiCo}_{0.8}\text{Cl}_{0.2}$  [33], S doped  $\text{SrIrO}_3$  [34], and P substituted  $\text{Co}_3\text{O}_4$  et al. [35]. Particularly, endowed with strong electronegativity and weak metal-F bond dissociation, [36–40] F containing compounds are prone to surface reconstruction. However, the inner correlation between surface reconstruction and OER mechanism of F incorporated perovskite oxides is still unclear and elusive.

Enlightened by the above, we propose an elegant F-anion incorporation approach to regulate the surface reconstruction on  $\text{LaNi}_{0.75}\text{Fe}_{0.25}\text{O}_3$  (LNFO) perovskite. Ni-Fe coupled perovskite is adopted for OER in view of the synergic effect between Ni and Fe [41–43]. We introduce F anion into LNFO perovskite by fluorination annealing at 200 °C, 250 °C, 300 °C, 350 °C, receiving LNFO-200 F, LNFO-250 F, LNFO-300 F, and LNFO-350 F electrocatalysts, respectively. Strong evidences from in-situ Raman spectroscopy and theoretical calculations unveil that F incorporation can induce dynamic surface reconstruction to create electrochemically active oxyhydroxide layer on perovskite oxide, which lowers the theoretical energy barrier of OER. The resultant LNFO-250 F electrocatalyst exhibits a remarkably enhanced OER activity relative to the pristine LNFO electrocatalyst, exhibiting an ultralow overpotential of 292 mV to achieve  $10 \text{ mA cm}^{-2}$ . As a result, the LNFO-250 F|Pt-C based electrolyzer delivers high performance and good durability. This study offers an operability of engineering surface reconstruction on perovskite oxide via anion regulation and provides a comprehensive understanding of underlying OER mechanism involving surface reconstruction.

## 2. Experimental section

### 2.1. Synthesis of F incorporated perovskites

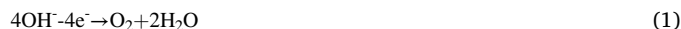
$\text{LaNi}_{0.75}\text{Fe}_{0.25}\text{O}_3$  (LNFO) perovskite was synthesized by a common sol-gel way. Stoichiometric amounts of  $\text{LaNO}_3 \cdot 6 \text{ H}_2\text{O}$ ,  $\text{Fe}(\text{NO}_3)_3 \cdot 9 \text{ H}_2\text{O}$ , and  $\text{Ni}(\text{NO}_3)_2 \cdot 6 \text{ H}_2\text{O}$  (analytical grade) chemicals were dissolved into a  $\text{HNO}_3$  solution, resulting in a clarified homogeneous solution. To stabilize metal ions, sequestering agents of citric acid and ethylenediamine tetraacetic acid were subsequently added at a molar ratio of 1: 1.5.  $\text{NH}_3 \cdot 6 \text{ H}_2\text{O}$  solution was employed to tune the pH value at  $\sim 7$ . After that, this solution was heat-treated on a hotplate stirrer at 200 °C until self-combustion happens, followed via calcination at 700 °C for 2 h to receive a LNFO powder. In a common procedure of fluorination, the LNFO and  $\text{NH}_4\text{F}$  powders were placed in two neighboring porcelain boats and was annealing at 200 °C, 250 °C, 300 °C and 350 °C for 2 h under Ar atmosphere, denoted as LNFO-200 F, LNFO-250 F, LNFO-300 F and LNFO-350 F.

### 2.2. Physicochemical characterizations

X-ray diffraction (XRD, Bruker, D8 Advance) using a Cu K $\alpha$  radiation was carried out in the  $2\theta$  range of  $10^\circ \sim 90^\circ$  to study crystal structures of electrocatalysts. The morphologies of electrocatalysts were characterized on a scanning electron microscopy (SEM, Hitachi SU8010). High-resolution transmission electron microscopy (HRTEM, Tecnai G260-300) were applied to investigate the detailed electrocatalyst microstructures. X-ray photoelectron spectroscopy (XPS, AXIS-His spectrometer) using a monochromatic Al K $\alpha$  source was carried out to understand surface chemical states of electrocatalysts. XPS spectra at the etching depths of approximately 3 nm, 6 nm, 9 nm, 12 nm and 15 nm were conducted. In addition, the XPS C 1s signal at 284.8 eV was adopted for calibration. For synchrotron radiation X-ray absorption spectroscopy (XAS), the electrocatalysts and standard samples of Ni and Fe K-edge were recorded at the 1W1B station of the Beijing Synchrotron Radiation Facility (BSRF). Raman spectra were conducted on a spectroscopy (Horiba Jobin Yvon S.A.S.) with a 532 nm excitation laser. A home-made spectro-electrochemical cell with three-electrode configuration was used to study the operando Raman spectra.

### 2.3. Electrochemical measurements

Electrochemical OER evaluation was performed in a three-electrode system using an electrochemical workstation (CHI 760E). KOH solution (1 M) served as the alkaline electrolyte. Graphite rod electrode was used as the counter electrode, while saturated calomel electrode was employed as the reference electrode. For preparation of the working electrode, electrocatalyst powder (80 mg) was dissolved into ethanol (9.5 mL) and Nafion solution (0.5 mL, Sigma-Aldrich), followed by ultrasound for 2 h to achieve an electrocatalyst dispersion. After that, stoichiometric catalyst dispersion was dropped on the polished glassy carbon (GC) working electrode using a pipetting gun to yield an electrocatalyst depositing of  $0.45 \text{ mg cm}^{-2}$ . Linear sweeping voltammogram (LSV) and cyclic voltammetry (CV) measurements were set at the sweep speed of  $10 \text{ mV s}^{-1}$ . Electrochemical impedance spectroscopy tests were carried out at 1.57 V vs. RHE in the frequency range of 0.1 MHz–0.1 Hz. Electrochemical double-layer capacitor ( $C_{dl}$ ) values were fitted via scanning CV at multiple sweep speeds ranging from 10 to  $140 \text{ mV s}^{-1}$ . Electrochemical active surface area (ECSA) could be calculated as follow:  $\text{ECSA} = C_{dl}/C_s$ , where  $C_s$  is the specific capacitance of flat surface area ( $40 \mu\text{F cm}^{-2}$ ). Additionally, all measured potentials were calibrated to the reversible hydrogen electrode (RHE) with 85 % iR correction. In a home-made two-electrode alkaline electrolyzer (1.0 M KOH electrolyte), LNFO-250 F@carbon cloth was applied as the anode, while commercial 20 w.t.% Pt/C@carbon cloth was employed as the cathode. The electrocatalyst powders were deposited on carbon cloth with a mass loading of  $1 \text{ mg cm}^{-2}$ . The anode and cathode reactions were expressed by Eq. 1 and Eq. 2, respectively.



To determine the Faraday efficiency of water splitting, a water displacement method was conducted to measure the volumes of the produced  $\text{O}_2$  and  $\text{H}_2$  gases [44].

### 2.4. Theoretical calculations

Density functional theory (DFT) calculations were conducted using the Vienna Ab initio Simulation Package (VASP) based on projector augmented wave (PAW) method [45,46]. The exchange-functional was addressed by the generalized gradient approximation (GGA) of Perdew-Burke-Ernzerhof (PBE) functional [47,48]. In view of the magnetic properties of Fe and Ni, spin-polarized calculations were adopted. To guarantee the accuracy of GGA, the Hubbard U values (employed as

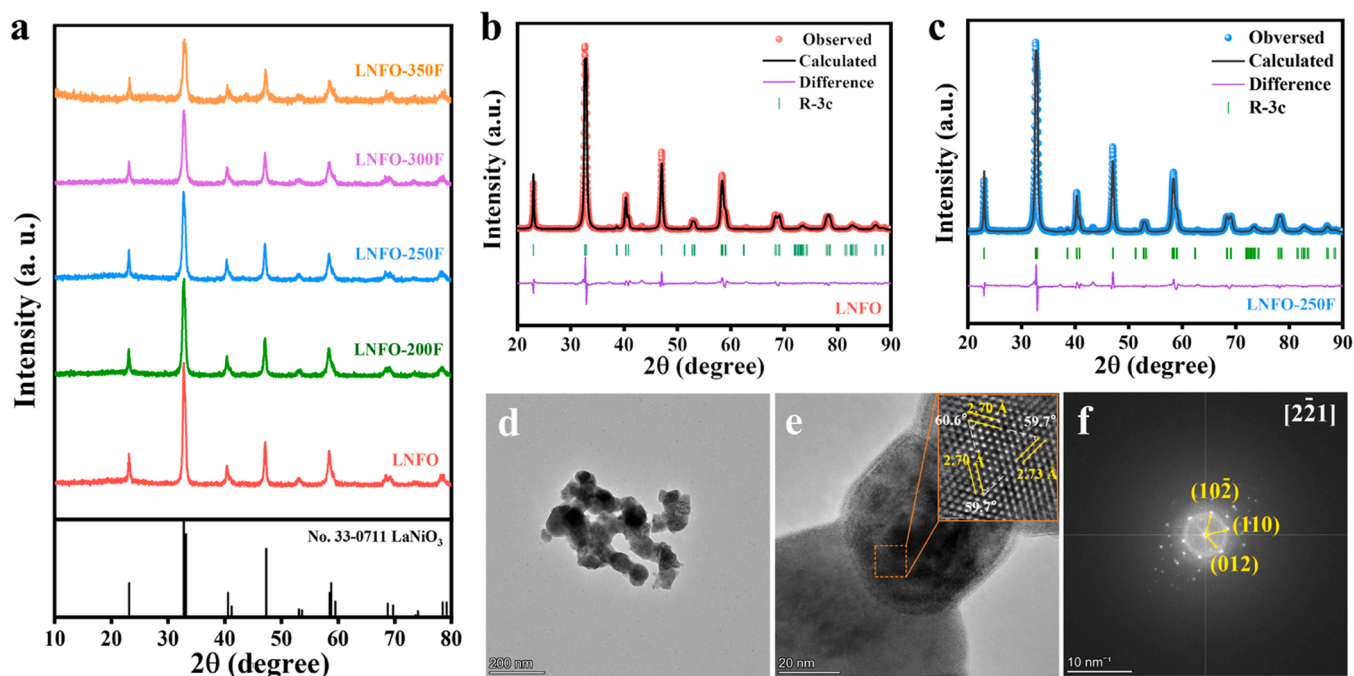


**Fig. 1.** (a) XRD patterns of LNFO, LNFO-200 F, LNFO-250 F, LNFO-300 F and LNFO-350 F powders; Rietveld refinement XRD patterns of (b) LNFO and (c) LNFO-250 F samples; (d) Low magnification TEM image, (e) High magnification TEM image and (f) Fast Fourier transform of LNFO-250 F sample.

U – J) of 4.0 and 6.4 for Fe and Ni were taken from literature [49]. An energy cutoff for the plane wave basis expansion of 400 eV, a force on each atom less than 0.05 eV/Å, and a convergence threshold of  $1 \times 10^{-4}$  eV in total energy were adopted. The  $p(4 \times 4)$  LaNiO<sub>3</sub> (001) surface was constructed, whereas  $\frac{1}{4}$  Ni was replaced by Fe to form  $p(4 \times 4)$  LaNi<sub>0.75</sub>Fe<sub>0.25</sub>O<sub>3</sub> (001) surface. (Ni<sub>0.75</sub>Fe<sub>0.25</sub>)OOH (001) was built on the surface of LaNi<sub>0.75</sub>Fe<sub>0.25</sub>O<sub>3</sub> (001), because the (Ni<sub>0.75</sub>Fe<sub>0.25</sub>)OOH (001) was thermodynamically stable [50]. Moreover, the substitution of O by F was implemented to simulate the F doping. The Brillouin zone was sampled with Monkhorst mesh of  $1 \times 1 \times 1$  on account of the large unit cell. The Gibbs free energies for adsorbed oxygen intermediates were corrected via zero-point energy and entropy [20].

### 3. Results and discussion

#### 3.1. Structural characterization

The pristine LaNi<sub>0.75</sub>Fe<sub>0.25</sub>O<sub>3</sub> (LNFO) perovskite was prepared via a sol-gel method [51]. Subsequently, the F incorporated LNFO perovskites were achieved after a facile fluorination annealing at 200 °C, 250 °C, 300 °C, 350 °C, denoted as LNFO-200 F, LNFO-250 F, LNFO-300 F, and LNFO-350 F, respectively. Crystalline structures of electrocatalyst powders were characterized by X-ray diffraction (XRD). As described in Fig. 1a, the as-prepared LNFO powder exhibits a rhombohedral perovskite structure (R-3c). After the fluorination treatment at various temperatures, the rhombohedral perovskite structure remains primarily unchanged (Fig. S1). Rietveld refinements were subsequently carried out on LNFO (Fig. 1b) and LNFO-250 F (Fig. 1c) powders to further analyze the detailed crystal structures. The simulated lattice parameters are summarized in Table S1. The unit cell volume of LNFO-250 F slightly reduces compared to LNFO, due to a smaller radius of fluorine anion replacing lattice oxygen.

Morphologies of the as-synthesized electrocatalysts were analyzed via scanning electron microscopy (SEM) and transmission electron microscopy (TEM). SEM analysis shows that the particles of all samples are well developed with dozens of nanometers in size (Fig. S2). Those particles connect with each other to form irregular aggregations (Fig. 1d), promising 3D connected networks for electron transfer and mass

transfer. Based on TEM analysis (Fig. S3), the obtained lattice spacings of the pristine LNFO are 2.70 Å and 3.79 Å, fairly corresponding to its (012) and (0–11) planes. In the case of LNFO-250 F, the lattice spacings are 2.70 Å and 2.73 Å, in line with (012) and (110) diffraction planes (Fig. 1e). Additionally, the fast Fourier transform (FFT) pattern agrees well with the  $[2-21]$  zone axis of LNFO-250 F trigonal perovskite (Fig. 1f).

#### 3.2. Oxygen evolution behavior

To investigate the effect of F incorporation on OER activity, electrochemical characterizations over LNFO, LNFO-200 F, LNFO-250 F, LNFO-300 F, LNFO-350 F and benchmark IrO<sub>2</sub> electrocatalysts were performed in O<sub>2</sub>-saturated 1.0 M KOH electrolyte with a conventional three-electrode system. As described in polarization sweeps of linear sweep voltammetry (LSV) (Fig. 2a), the pristine LNFO electrocatalyst displays a moderate OER activity, requiring an overpotential of 396 mV to receive the current density of 10 mA cm<sup>-2</sup> (Fig. 2b). After F incorporation, the overpotentials noticeably reduce. Among them, the LNFO-250 F electrocatalyst demonstrates the best OER activity with an extremely low overpotential of 292 mV at 10 mA cm<sup>-2</sup>. Notably, the OER activity of LNFO-250 F electrocatalyst is favorably compared to the benchmark IrO<sub>2</sub> electrocatalyst and those recently reported perovskite electrocatalysts (LaNi<sub>0.8</sub>Fe<sub>0.2</sub>O<sub>3</sub> [23], La<sub>0.9</sub>Ce<sub>0.1</sub>NiO<sub>3</sub> [26], LaNiO<sub>3</sub>/NiO [52], LaCo<sub>0.75</sub>Fe<sub>0.25</sub>O<sub>3</sub> [53], La<sub>0.6</sub>Sr<sub>0.4</sub>(CoFeMnNiMg)O<sub>3</sub> [20], V<sub>Fe,Sr</sub>-La<sub>x</sub>Sr<sub>1-x</sub>CoO<sub>3</sub> [54], Ba<sub>0.5</sub>Sr<sub>0.5</sub>Co<sub>0.8</sub>Fe<sub>0.2</sub>O<sub>3-δ</sub> [10], SrNb<sub>0.1</sub>Co<sub>0.7</sub>Fe<sub>0.2</sub>O<sub>3-δ</sub> [55], PrBaCo<sub>2</sub>O<sub>5+δ</sub> [56], PrBa<sub>0.5</sub>Sr<sub>0.5</sub>Co<sub>1.55</sub>Fe<sub>0.45</sub>O<sub>5+δ</sub> [57], PrBa<sub>0.5</sub>Sr<sub>0.5</sub>Co<sub>1.5</sub>Fe<sub>0.5</sub>O<sub>5+δ</sub> [11], La<sub>2</sub>NiMnO<sub>6</sub> [58] Fig. S4). Interestingly, the LSV sweeps (Fig. 2a) together with the detailed cyclic voltammetry (CV) sweeps (Fig. S5) show that the distinct redox peaks preceding the OER process occur on the F-incorporated LNFO electrocatalysts rather than the pristine LNFO, which is likely ascribed to the electrochemical transformation of Ni<sup>2+</sup>/Ni<sup>3+</sup> [59,60]. These redox peaks suggest that the F-incorporation may induce newly-created species prior to OER process.

The OER kinetics of electrocatalysts were assessed via Tafel slopes and electrochemical impedance spectroscopy (EIS). In Tafel plots (Fig. 2c), the fitted slope of LNFO-250 F electrocatalyst is 58.8 mV dec<sup>-1</sup>, smaller than those of other studied electrocatalysts, e.g. 132.3 mV dec<sup>-1</sup>

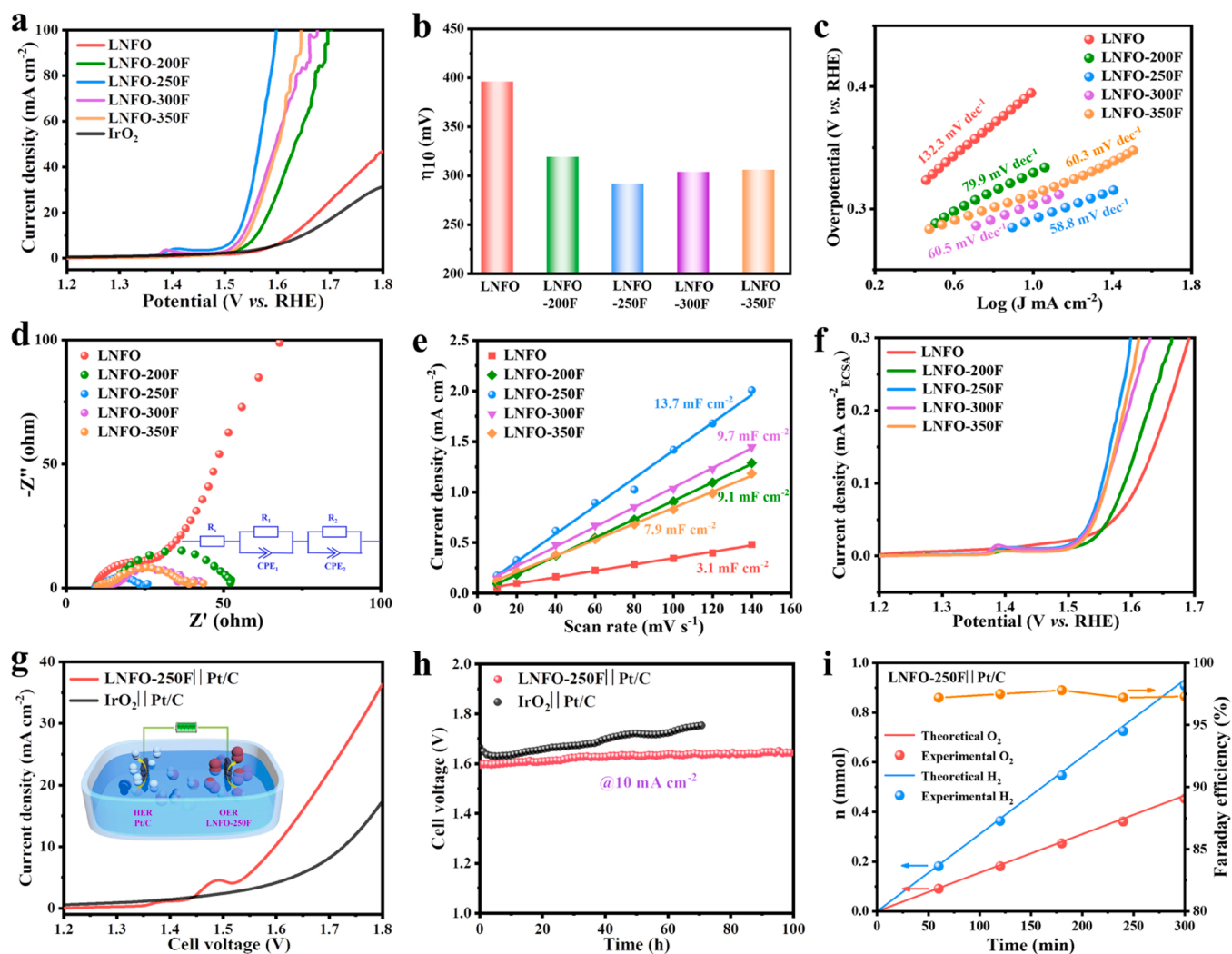


**Fig. 2.** (a) LSV polarization curves, (b) Overpotential values at  $10 \text{ mA cm}^{-2}$ , (c) Tafel slopes extracted from LSV curves, (d) Nyquist plots, (e) Double-layer capacitances, (f) ECSA-normalized intrinsic activities of LNFO, LNFO-200 F, LNFO-250 F, LNFO-300 F, LNFO-350 F in  $1.0 \text{ M KOH}$  electrolyte; (g) Polarization curves, (h) Chronopotentiometry curves of alkaline water splitting devices using LNFO-250 F||Pt-C and  $\text{IrO}_2$ ||Pt/C coupled electrodes, and (i) Faraday efficiency of LNFO-250 F||Pt-C based water splitting device conducted at  $10 \text{ mA cm}^{-2}$ .

of pristine LNFO,  $79.9 \text{ mV dec}^{-1}$  of LNFO-200 F,  $60.5 \text{ mV dec}^{-1}$  of LNFO-300 F and  $60.3 \text{ mV dec}^{-1}$  of LNFO-350 F. This indicates that the LNFO-250 F electrocatalyst yields a faster electrocatalytic kinetics towards OER than other electrocatalysts. Furthermore, the F-incorporation considerably reduces the polarization resistance of LNFO (Fig. 2d), fairly agreeing with the trend of OER activity. In addition, all EIS curves consist of two overlapped arcs, implying that there might be two rate-limiting processes. Equivalent circuit of  $R_s(R_1/CPE_1)(R_2/CPE_2)$  is thereby adopted to simulate the spectra, where  $R_s$ ,  $R_1$ , and  $R_2$  are, respectively, the resistance of electrolyte, the resistance of electrode texture as well as the resistance of charge transfer [33]. As illustrated in Table S2, the LNFO-250 F electrocatalyst possesses the smallest charge transfer resistance of  $11.9 \Omega$ , suggestive of the fastest charge transfer kinetics for OER.

By conducting CV sweeps at different scan rates from  $10 \text{ mV s}^{-1}$  to  $140 \text{ mV s}^{-1}$  (Fig. S6), the derived double-layer capacitances ( $C_{dl}$ ) of LNFO, LNFO-200 F, LNFO-250 F, LNFO-300 F and LNFO-350 F are  $3.1 \text{ mF cm}^{-2}$ ,  $9.1 \text{ mF cm}^{-2}$ ,  $13.7 \text{ mF cm}^{-2}$ ,  $9.7 \text{ mF cm}^{-2}$  and  $7.9 \text{ mF cm}^{-2}$ , respectively (Fig. 2e). The largest  $C_{dl}$  over LNFO-250 F electrocatalyst denotes the most active sites among those studied electrocatalysts. Furthermore, the LSV curves normalized via electrochemical active surface area (ECSA) are provided in Fig. 2 f. One can see that the LNFO-

250 F electrocatalyst exhibits the largest specific current density as well, indicative of the highest intrinsic activity towards OER.

To demonstrate the actual feasibility, a two-electrode water splitting system was assembled, consisting of LNFO-250 F anode,  $1.0 \text{ M KOH}$  solution electrolyte, and commercial Pt/C cathode (Fig. 2 g). For comparison, the electrolyzer using benchmark  $\text{IrO}_2$ ||Pt/C electrode was also prepared. To achieve the electrolytic current density of  $10 \text{ mA cm}^{-2}$ , a reduced cell voltage of  $1.58 \text{ V}$  is required for the LNFO-250 F||Pt-C based electrolyzer, compared to the  $\text{IrO}_2$ ||Pt/C based electrolyzer ( $1.65 \text{ V}$  for  $10 \text{ mA cm}^{-2}$ ). More importantly, the electrolyzer using LNFO-250 F||Pt-C electrode demonstrates an excellent durability during practical operation. The benchmark  $\text{IrO}_2$ ||Pt/C based electrolyzer shows gradual degradation during the continuously electrochemical operation. By contrast, a tiny decay in cell voltage (less than  $50 \text{ mV}$ ) is obtained after electrolyzing for  $100 \text{ h}$  (Fig. 2 h). In addition, the LNFO-250 F||Pt-C based electrolyzer almost remains stable at a high applied current density of  $100 \text{ mA cm}^{-2}$  (Fig. S7). Fig. 2i shows that the experimental  $\text{O}_2$  and  $\text{H}_2$  production are compared to the theoretical data. At a current density of  $10 \text{ mA cm}^{-2}$ , the faradaic efficiencies of the LNFO-250 F||Pt-C based electrolyzer are approximately  $97 \%$ .



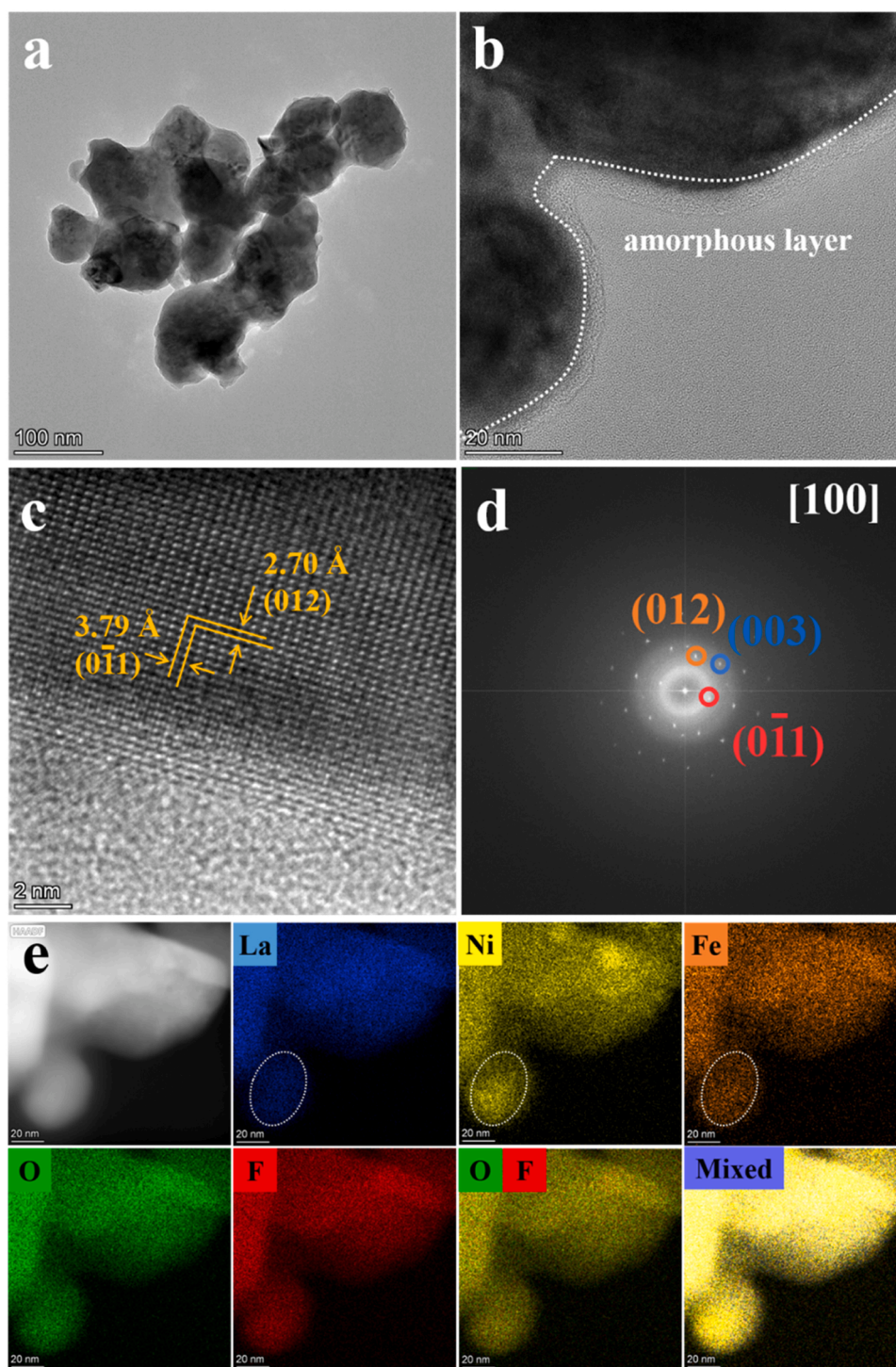


**Fig. 3.** (a) Low magnification TEM image, High magnification TEM images with different scale bars of (b) 20 nm and (c) 2 nm, (d) Fast Fourier transform, and (e) Elemental mappings of LNFO-250 F electrocatalyst post-OER.

### 3.3. Dynamic surface reorganization

To probe the potential surface evolution and structural change happened during OER process, ex-situ and in-situ structure characterizations were implemented. Examined by TEM, the morphology of the post-OER LNFO perovskite remains stable (Fig. S8). The observed interplanar spacing of 3.82 Å is well assigned to the (101) plane of LNFO. In contrast, although the overall microstructure is maintained (Fig. 3a), a stretch of amorphous layer with a thickness of ~5 nm is generated on the near-surface of the post-OER LNFO-250 F

electrocatalyst (Fig. 3b). Under the amorphous layer, the retentive LNFO-250 F perovskite crystalline structure is confirmed, as evidenced via the lattice spacings (Fig. 3c) and FFT pattern (Fig. 3d). Additionally, elemental mapping analysis illustrates that the surface reconstruction of LNFO-250 F is accompanied by the richness of Ni, Fe rather than La (Fig. 3e). By comparison, we can speculate that F incorporation triggers the surface structural transformation of perovskite oxide.

As revealed, the electronic structure of amorphous layer is closely related with OER mechanism [61]. X-ray photoelectron spectroscopy (XPS) spectra of LNFO and LNFO-250 F electrocatalysts before and after

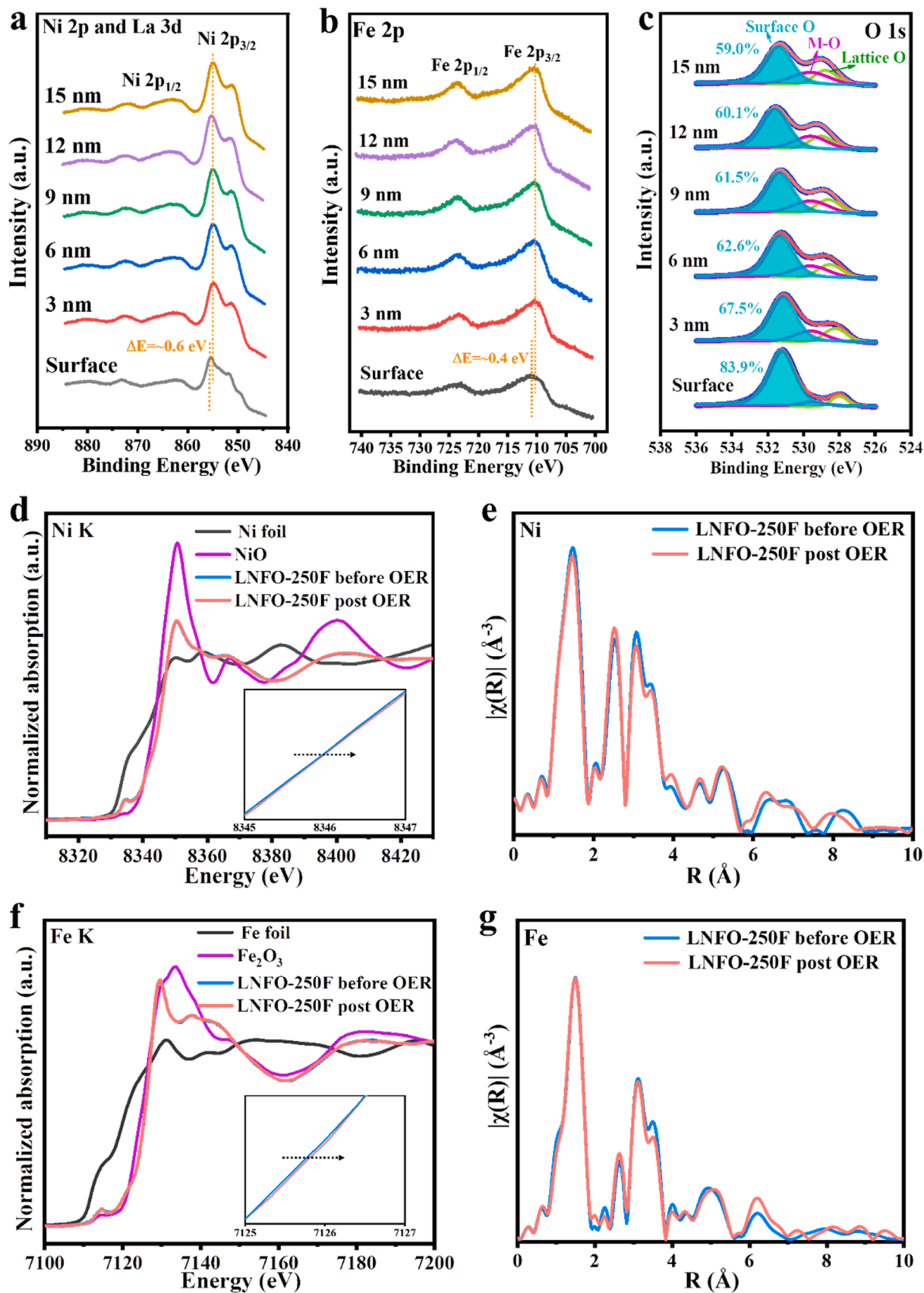
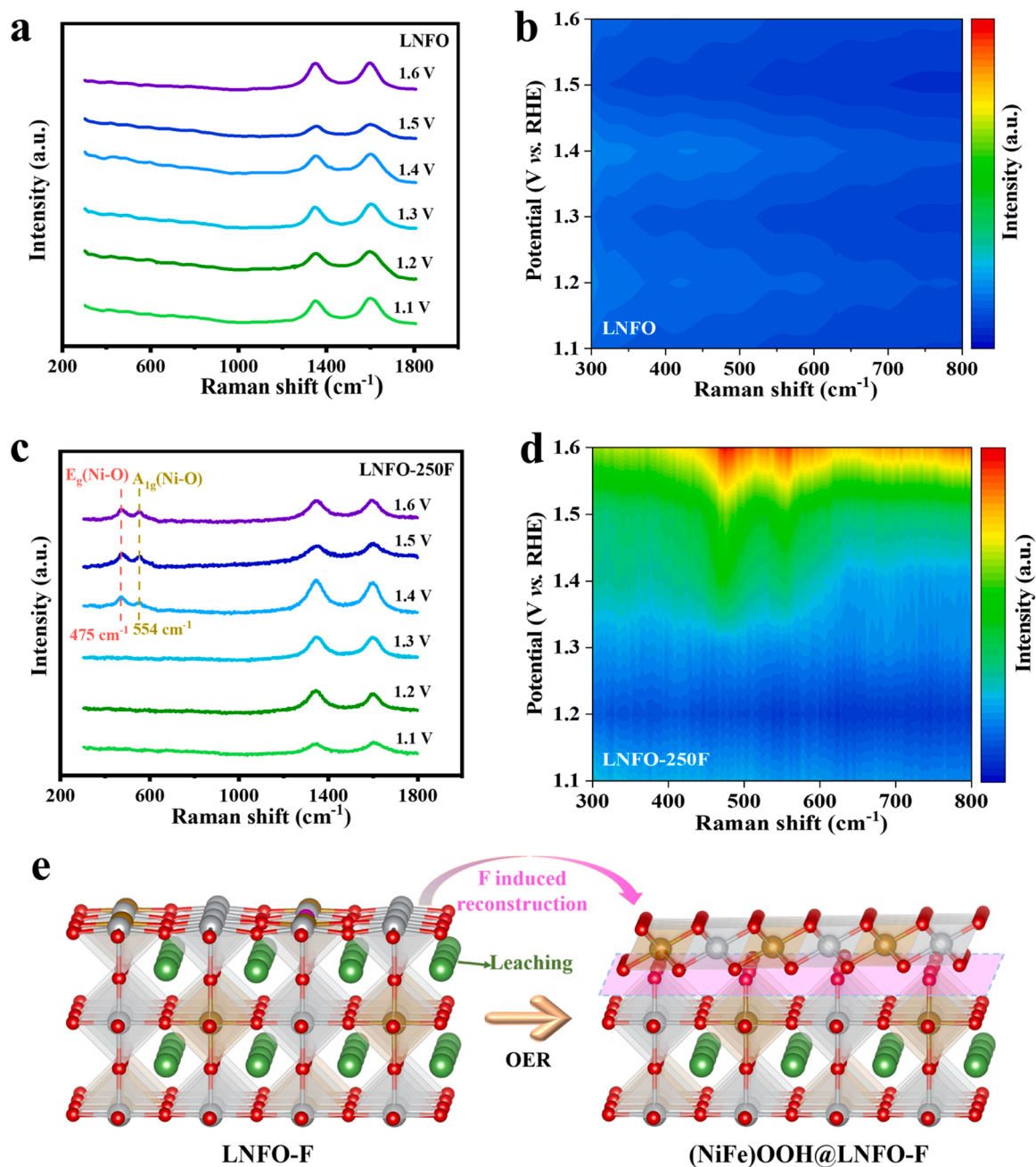


Fig. 4. Depth analysis of XPS spectra from surface to 15 nm for LNFO-250 F electrocatalyst post-OER, (a) Ni 2p&La 3d, (b) Fe 2p, (c) O 1s; (d) XANES spectra of Ni K-edge, (e) EXAFS spectra of Ni in R space, (f) XANES spectra of Fe K-edge, (g) EXAFS spectra of Fe in R space for LNFO-250 F electrocatalyst before and post OER.



**Fig. 5.** (a) In-situ Raman spectra at cycle applied potentials from 1.1 V to 1.6 V and (b) Corresponding contour plots of in-situ Raman spectra for LNFO electrocatalyst; (c) In-situ Raman spectra at cycle applied potentials from 1.1 V to 1.6 V and (d) Corresponding contour plots of in-situ Raman spectra for LNFO-250 F electrocatalyst; (e) Proposed F induced surface reconstruction behavior on perovskite oxide (La atom: green, Ni atom: light white, Fe atom: brown, F atom: purple, O atom: red).

OER operation were then investigated. As shown in Fig. S9, the characteristic peaks of Ni 2p and Fe 2p of LNFO have no significant shifts before and after OER operation. But for LNFO-250 F (Fig. S10), the Ni 2p peaks located at 857.2 eV and 853.6 eV are indexed to Ni<sup>I</sup> and Ni<sup>II</sup> species before OER [62], which transform into the typical Ni<sup>III</sup> peak at 855.7 eV after OER [23]. Meanwhile, the Fe 2p<sub>3/2</sub> core-level peak of LNFO-250 F shifts to a high binding energy with about 0.4 eV after OER, indicating that a relatively higher valence state of Fe is received in the post-OER LNFO-250 F electrocatalyst. Moreover, the O 1s spectra can be deconvoluted into lattice O at ~528.7 eV, perovskite termination M-O at ~529.5 eV and surface O at ~531.3 eV [52,63]. The concentration of surface oxygen species of LNFO-250 F is significantly enhanced after OER process, indicating the improved adsorption

capacity of oxygen intermediates for OER. Additionally, the XPS spectra of LNFO-250 F with different operation time remains almost constant over time, suggesting that the amorphous layer is likely chemically stable during OER process. We further conduct XPS depth profiling from surface to 15 nm in depth for the post-OER LNFO-250 F electrocatalyst. As shown in Fig. 4a, the Ni 2p<sub>3/2</sub> peak in near surface (~3 nm) shifts to higher binding energy (about 0.4 eV) compare to other depths. Similar pattern is also identified in Fe 2p<sub>3/2</sub> spectra (Fig. 4b). These positive shifts denote that both the valence states of nickel and iron in the near surface are improved by electrochemical OER operation. Furthermore, it is clearly seen that the relative concentration of surface oxygen also remarkably increases in the near surface.

To further explore the Ni 3d and Fe 3d states, X-ray absorption near-



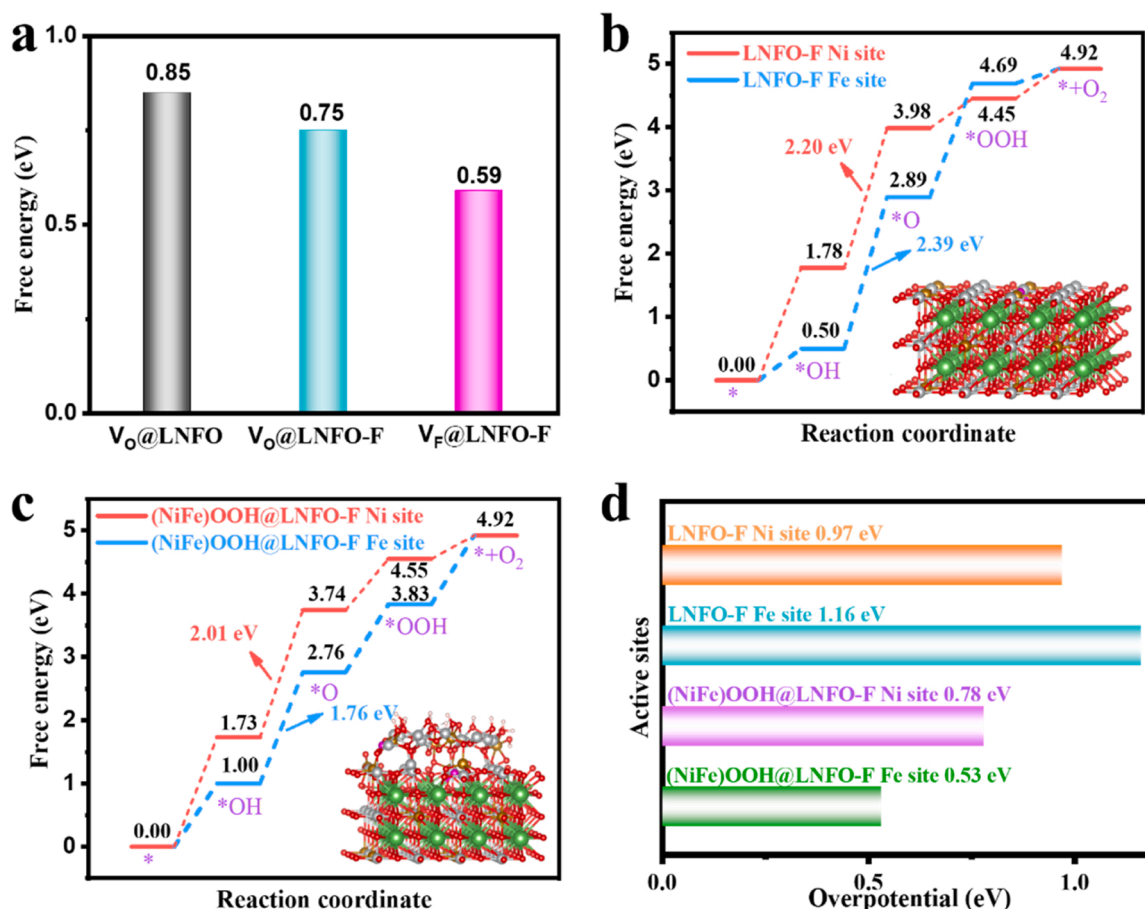


**Fig. 6.** DFT calculations. (a) Vacancy formation energy on LNFO and LNFO-F surface; OER free energy diagram of (b) the LNFO-F and (c) the surface reconstructed (NiFe)OOH@LNFO-F; and (d) Corresponding theoretical overpotentials.

edge structure (XANES) spectroscopy and extended X-ray absorption fine structure (EXAFS) measurements at Ni K-edge and Fe K-edge of the LNFO-250 F electrocatalyst before and after OER process were performed. One can see that both XANES Ni K-edge (Fig. 4d) and Fe K-edge (Fig. 4f) undergo little shift to higher energy, implying that the apparent oxidation states of Ni and Fe are oxidized via OER electrocatalysis [52]. These oxidized Ni and Fe states are well consistent with the results of XPS analysis. In addition, derived from the EXAFS Ni (Fig. 4e) and Fe (Fig. 4g) spectroscopy of LNFO-250 F, the fitted path of Ni-O and Fe-O shorten from 1.95 to 1.94 Å and 1.94–1.93 Å, respectively, after OER process (Table S3). The detailed wavelet transform counter map of Ni and Fe are depicted in Fig. S11, to visualize coordination environment. The changes of morphology and chemical state evidentially confirm the surface reconstruction of LNFO-250 F electrocatalyst after OER operation.

To reveal the dynamic surface reorganization process, operando Raman measurements during OER process were employed (Fig. S12). With the applied potential increasing from 1.1 V to 1.6 V (vs. reversible hydrogen electrode, RHE), no other peaks are detected except the characteristic peaks of the pristine LNFO, as shown in Raman spectra (Fig. 5a) and corresponding contour plots (Fig. 5b). On the contrary, the potential-dependent Raman spectra (Fig. 5c) and contour plots (Fig. 5d) of F-incorporated LNFO-250 F clearly show that when the applied potentials are higher than 1.3 V vs. RHE, two strong Raman signals at around 475 and 554  $\text{cm}^{-1}$  are gained, respectively, corresponding to Ni-O bending and NiOOH stretching vibration [64–66]. These results evidently show that the F incorporation can induce surface reconstruction of LNFO perovskite during OER process, yielding a new phase of electrochemically active oxyhydroxide. In addition, the Raman signals

of Ni-O bending and NiOOH stretching vibration for LNFO-250 F decrease with the reduced potential in a cycling process (Fig. S13), suggesting a reversible electrochemical transformation between  $\text{Ni}^{2+}/\text{Ni}^{3+}$ . This is also confirmed by CV curves in Fig. S5. Based on the analysis of TEM, XPS, XAS, and operando Raman, the electrochemically driven surface reconstruction on F incorporated LNFO as a formation of perovskite-oxyhydroxide core-shell heterostructure is verified. As proposed in Fig. 5e, the (NiFe) coordination polyhedrons on perovskite surface undergo a reconstruction process to form (NiFe)OOH, meanwhile the surface La cations may leach out from perovskite [67].

### 3.4. Oxygen evolution mechanism

Density functional theory (DFT) calculations were carried out to deepen the understanding of surface reconstruction and intrinsic activity of F incorporated LNFO electrocatalyst. It is well accepted that the vacancy formation enthalpy of perovskites plays as an essential cause of surface reconstruction. The low vacancy formation energy usually facilitates the structural rearrangement kinetics [26,62]. For comparison, we build the architectures of surface oxygen vacancy in LNFO (Fig. S14), surface oxygen vacancy in F-doped LNFO (LNFO-F), and surface fluorine vacancy in LNFO-F (Fig. S15). The calculated vacancy formation energies are illustrated in Fig. 6a. The formation energy of surface oxygen vacancy in LNFO is 0.85 eV, which is higher than those of surface oxygen vacancy in F-doped LNFO (LNFO-F) and surface fluorine vacancy in LNFO-F (0.59 eV). This indicates that the vacancies, especially fluorine vacancy, in LNFO-F are readily generated relative to the oxygen vacancy in LNFO, ultimately in favor of structural rearrangement.

Moreover, a widely accepted four electron-proton coupled OER



mechanism involves the sequential process of  $* \rightarrow *OH \rightarrow *O \rightarrow *OOH \rightarrow *$  [68]. On the basis of the electrochemically driven surface reconstruction, (NiFe)OOH@LNFO-F heterostructure was adopted to predict the real active sites. For comparison, the LNFO-F surface was also built to compare the OER activity. Considering the strong interaction between transition metal 3d orbital and O 2p orbital, oxygen intermediates are prone to be adsorbed on Ni (or Fe) sites of LNFO-F and (NiFe)OOH@LNFO-F. These adsorbed configurations for OER process are presented in Figs. S16–S19. The rate-limiting step with the largest energy barrier of OER for both LNFO-F (Fig. 6b) and (NiFe)OOH@LNFO-F (Fig. 6c) is the electrochemical conversion from  $*OH$  to  $*O$ . The calculated energy barriers over surface Ni site and Fe site of LNFO-F are 2.20 eV and 2.39 eV, respectively. In the case of (NiFe)OOH@LNFO-F, the energy barriers on surface Ni site and Fe site reduce to 2.01 eV and 1.76 eV. It is concluded that the (NiFe)OOH@LNFO-F heterostructure with lower overpotentials guarantees higher OER activity compared to the individual LNFO-F surface (Fig. 6d), fairly agreeing with the results of electrochemical measurements. Consequently, F incorporation into LNFO electrocatalyst with low vacancy formation energy activates the surface reconstruction, resulting in electrochemically active oxyhydroxide-perovskite heterostructure. Nevertheless, the excessive F incorporation may lead to low electronic conductivity [69,70], potentially impeding the OER process.

#### 4. Conclusions

In summary, we have developed an effective and effortless strategy of engineering anion defect on perovskite oxide to trigger the dynamic surface reconstruction for OER. The resultant fluorine incorporated LNFO-250 F electrocatalyst, delivering a small overpotential of 292 mV at 10 mA cm<sup>-2</sup> and a low Tafel slope of 58.8 mV dec<sup>-1</sup>, is more active for OER than the pristine LNFO electrocatalyst and the commercial IrO<sub>2</sub> electrocatalyst. Moreover, the LNFO-250 F||Pt-C based electrolyzer shows a good durability over 100 h under real operation conditions. According to the experimental and theoretical analysis, fluorine incorporated LNFO perovskite with low vacancy formation energy trigger surface transformation process. As a result, this formed oxyhydroxide-perovskite heterostructure efficiently lowers the energy barrier of OER. This protocol sheds light on rationally engineering surface reconstruction on perovskite electrocatalysts for water oxidation.

#### CRedit authorship contribution statement

**Jing Zhang:** Data curation, Formal analysis, Investigation, Writing – original draft. **Yu Ye:** Data curation, Investigation. **Bo Wei:** Methodology, Software. **Feng Hu:** Formal analysis. **Longtao Sui:** Investigation. **Huangwei Xiao:** Investigation. **Liangqi Gui:** Software. **Jian Sun:** Methodology. **Beibei He** and **Ling Zhao:** Formal analysis, Funding acquisition, Supervision, Writing – review & editing.

#### Declaration of Competing Interest

The authors declare that they have no known competing financial interests or personal relationships that could have appeared to influence the work reported in this paper.

#### Data availability

The data that has been used is confidential.

#### Acknowledgements

We are grateful for financial support from National Natural Science Foundation of China (No. 22075256 & No. 21975229), Zhejiang Provincial Natural Science Foundation of China (No. LY23E020004 & No. LY23B030004), and Shenzhen Science and Technology Program (No.

JCYJ20220530162403008).

#### Appendix A. Supporting information

Supplementary materials are available free of charge. Supplementary data associated with this article can be found in the online version at doi:10.1016/j.apcatb.2023.122661.

#### References

- [1] S.L. Zhao, Y.C. Yang, Z.Y. Tang, Insight into structural evolution, active sites, and stability of heterogeneous electrocatalysts, *Angew. Chem. Int. Ed.* 61 (2022), e202110186.
- [2] L.K. Gao, X. Cui, C.D. Sewell, J. Li, Z.Q. Lin, Recent advances in activating surface reconstruction for the high-efficiency oxygen evolution reaction, *Chem. Soc. Rev.* 50 (2021) 8428–8469.
- [3] H.N. Sun, S.Z. Song, X.M. Xu, J. Dai, J. Yu, W. Zhou, Z.P. Shao, W.O.C. Jung, Recent progress on structurally ordered materials for electrocatalysis, *Adv. Energy Mater.* 11 (2021), 2101937.
- [4] H.N. Sun, X.M. Xu, Y.F. Song, W. Zhou, Z.P. Shao, Designing high-valence metal sites for electrochemical water splitting, *Adv. Funct. Mater.* 31 (2021), 2009779.
- [5] M.J. Choi, T.L. Kim, J.K. Kim, T.H. Lee, S.A. Lee, C. Kim, K. Hong, C.W. Bark, K. T. Ko, H.W. Jang, Enhanced oxygen evolution electrocatalysis in strained A-site cation deficient LaNiO<sub>3</sub> perovskite thin films, *Nano Lett.* 20 (2020) 8040–8045.
- [6] N. Yao, G.W. Wang, H.N. Jia, J.L. Yin, H.J. Cong, S.L. Chen, W. Luo, Intermolecular energy gap-induced formation of high-valent cobalt species in CoOOH surface layer on cobalt sulfides for efficient water oxidation, *Angew. Chem. Int. Ed.* 61 (2022), e202117178.
- [7] H.N. Sun, X.M. Xu, H. Kim, W.C. Jung, W. Zhou, Z.P. Shao, Electrochemical water splitting: bridging the gaps between fundamental research and industrial applications, *Energy Environ. Mater.* (2022), e12441.
- [8] H.N. Sun, L.L. Li, Y.H. Chen, H. Kim, X.M. Xu, D.Q. Guan, Z.W. Hu, L.J. Zhang, Z. P. Shao, W.C. Jung, Boosting ethanol oxidation by NiOOH-CuO nano-heterostructure for energy-saving hydrogen production and biomass upgrading, *Appl. Catal. B Environ.* 325 (2023), 122388.
- [9] K.A. Stoerzinger, L. Qiao, M.D. Biegalski, Y. Shao-Horn, Orientation-dependent oxygen evolution activities of rutile IrO<sub>2</sub> and RuO<sub>2</sub>, *J. Phys. Chem. Lett.* 5 (2014) 1636–1641.
- [10] J. Suntivich, K.J. May, H.A. Gasteiger, J.B. Goodenough, Y. Shao-Horn, A perovskite oxide optimized for oxygen evolution catalysis from molecular orbital principles, *Science* 334 (2011) 1383–1385.
- [11] Y.M. Zhu, Z.Y. He, Y.M. Choi, H.J. Chen, X.B. Li, B.T. Zhao, Y. Yu, H. Zhang, K. A. Stoerzinger, Z.X. Feng, Y. Chen, M.L. Liu, Tuning proton-coupled electron transfer by crystal orientation for efficient water oxidation on double perovskite oxides, *Nat. Commun.* 11 (2020) 4299.
- [12] H. Lee, O. Gwon, K. Choi, L.J. Zhang, J. Zhou, J. Park, J.W. Yoo, J.Q. Wang, J. H. Lee, G. Kim, Enhancing bifunctional electrocatalytic activities via metal d-band center lift induced by oxygen vacancy on the subsurface of perovskites, *ACS Catal.* 10 (2020) 4664–4670.
- [13] S.V. Porokhin, V.A. Nikitina, D.A. Aksyonov, D.S. Filimonov, E.M. Pazhetnov, I. V. Mikhaylov, A.M. Abakumov, Mixed-cation perovskite La<sub>0.6</sub>Ca<sub>0.4</sub>Fe<sub>0.7</sub>Ni<sub>0.3</sub>O<sub>2.9</sub> as a stable and efficient catalyst for the oxygen evolution reaction, *ACS Catal.* 11 (2021) 8338–8348.
- [14] Y.N. Zhou, F.G. Wang, Y.N. Zhen, J. Nan, B. Dong, Y.M. Chai, Crystal facet engineering of perovskite cobaltite with optimized electronic regulation for water splitting, *Sci. China Mater.* 65 (2022) 2665–2674.
- [15] X. Cheng, E. Fabbri, Y. Yamashita, I.E. Castelli, B. Kim, M. Uchida, R. Haumont, I. Puente-Orench, T.J. Schmidt, Oxygen evolution reaction on perovskites: A multieffect descriptor study combining experimental and theoretical methods, *ACS Catal.* 8 (2018) 9567–9578.
- [16] E. Marelli, J. Gazquez, E. Poghosyan, E. Muller, D.J. Gawryluk, E. Pomjakushina, D. Sheptyakov, C. Piamonteze, D. Aegerter, T.J. Schmidt, M. Medarde, E. Fabbri, Correlation between oxygen vacancies and oxygen evolution reaction activity for a model electrode: PrBaCo<sub>2</sub>O<sub>5+δ</sub>, *Angew. Chem. Int. Ed.* 60 (2021) 14609–14619.
- [17] Y.L. Pan, X.M. Xu, Y.J. Zhong, L. Ge, Y.B. Chen, J.P.M. Veder, D.Q. Guan, R. O'Hayre, M.R. Li, G.X. Wang, H. Wang, W. Zhou, Z.P. Shao, Direct evidence of boosted oxygen evolution over perovskite by enhanced lattice oxygen participation, *Nat. Commun.* 11 (2020) 2002.
- [18] X.M. Xu, Y.L. Pan, J. Zhong, C.L. Shi, D.Q. Guan, L. Ge, Z.W. Hu, Y.Y. Ge, H.J. Lin, C.T. Chen, H. Wang, S.P. Jiang, Z.P. Shao, New undisputed evidence and strategy for enhanced lattice-oxygen participation of perovskite electrocatalyst through cation deficiency manipulation, *Adv. Sci.* 9 (2022), 2200530.
- [19] J.W. Zhao, H. Zhang, C.F. Li, X. Zhou, J.Q. Wu, F. Zeng, J.W. Zhang, G.R. Li, Key roles of surface Fe sites and Sr vacancies in the perovskite for an efficient oxygen evolution reaction via lattice oxygen oxidation, *Energy, Environ. Sci.* 15 (2022) 3912–3922.
- [20] L.N. Tang, Y.L. Yang, H.Q. Guo, Y. Wang, M.J. Wang, Z.Q. Liu, G.M. Yang, X.Z. Fu, Y. Luo, C.X. Jiang, Y.R. Zhao, Z.P. Shao, Y.F. Sun, High configuration entropy activated lattice oxygen for O<sub>2</sub> formation on perovskite electrocatalyst, *Adv. Funct. Mater.* 32 (2022) 2112157.
- [21] J.S. Liu, E.D. Jia, L. Wang, K.A. Stoerzinger, H. Zhou, C.S. Tang, X.M. Yin, X. He, E. Bousquet, M.E. Bowden, A.T.S. Wee, S.A. Chambers, Y.G. Du, Tuning the

- electronic structure of  $\text{LaNiO}_3$  through alloying with strontium to enhance oxygen evolution activity, *Adv. Sci.* 6 (2019), 1901073.
- [22] L. Wang, P. Adiga, J.L. Zhao, W.S. Samarakoon, K.A. Stoerzinger, S.R. Spurgeon, B. E. Matthews, M.E. Bowden, P.V. Sushko, T.C. Kaspar, G.E. Sterbinsky, S.M. Heald, H. Wang, L.W. Wangoh, J.P. Wu, E.J. Guo, H.J. Qian, J.O. Wang, T. Varga, S. Thevuthasan, Z.X. Feng, W.L. Yang, Y.G. Du, S.A. Chambers, Understanding the electronic structure evolution of epitaxial  $\text{LaNi}_{1-x}\text{Fe}_x\text{O}_3$  thin films for water oxidation, *Nano Lett.* 21 (2021) 8324–8331.
  - [23] H.P. Wang, J. Wang, Y.C. Pi, Q. Shao, Y.M. Tan, X.Q. Huang, Double perovskite  $\text{LaFe}_x\text{Ni}_{1-x}\text{O}_3$  nanorods enable efficient oxygen evolution electrocatalysis, *Angew. Chem. Int. Ed.* 58 (2019) 2316–2320.
  - [24] T.H. Shen, L. Spillane, J. Vavra, T.H.M. Pham, J.Y. Peng, Y. Shao-Horn, V. Tileli, Oxygen evolution reaction in  $\text{Ba}_{0.5}\text{Sr}_{0.5}\text{Co}_{0.8}\text{Fe}_{0.2}\text{O}_{3-\delta}$  aided by intrinsic Co/Fe spinel-like surface, *J. Am. Chem. Soc.* 142 (2020) 15876–15883.
  - [25] C. Baeumer, J. Li, Q.Y. Lu, A.Y.L. Liang, L. Jin, H.P. Martins, T. Duchon, M. Gloss, S.M. Gericke, M.A. Wohlgemuth, M. Giesen, E.E. Penn, R. Dittmann, F. Gunkel, R. Waser, M. Bajdich, S. Nemsak, J.T. Mefford, W.L.C. Chueh, Tuning electrochemically driven surface transformation in atomically flat  $\text{LaNiO}_3$  thin films for enhanced water electrolysis, *Nat. Mater.* 20 (2021) 674.
  - [26] Y. Sun, R. Li, X.X. Chen, J. Wu, Y. Xie, X. Wang, K.K. Ma, L. Wang, Z. Zhang, Q. L. Liao, Z. Kang, Y. Zhang, A-site management prompts the dynamic reconstructed active phase of perovskite oxide OER catalysts, *Adv. Energy Mater.* 11 (2021), 2003755.
  - [27] Y. Zhu, D.D. Liu, H.J. Jing, F. Zhang, X.B. Zhang, S.Q. Hu, L.M. Zhang, J.Y. Wang, L.X. Zhang, W.H. Zhang, B.J. Pang, P. Zhang, F.T. Fan, J.P. Xiao, W. Liu, X.F. Zhu, W.S. Yang, Oxygen activation on Ba-containing perovskite materials, *Sci. Adv.* 8 (2022), eabn4072.
  - [28] P.P. Lopes, D.Y. Chung, X. Rui, H. Zheng, H.Y. He, P. Martins, D. Strmcnik, V. R. Stamenkovic, P. Zapol, J.F. Mitchell, R.F. Klie, N.M. Markovic, Dynamically stable active sites from surface evolution of perovskite materials during the oxygen evolution reaction, *J. Am. Chem. Soc.* 143 (2021) 2741–2750.
  - [29] H.Y. Li, Y.B. Chen, J.J. Ge, X.H. Liu, A.C. Fisher, M.P. Sherburne, J.W. Ager, Z. J. Xu, Active phase on  $\text{SrCo}_{1-x}\text{Fe}_x\text{O}_{3-\delta}$  ( $0 < x \leq 0.5$ ) perovskite for water oxidation: reconstructed surface versus remaining bulk, *JACS Au* 1 (2021) 108–115.
  - [30] Y.B. Chen, Y.M. Sun, M.Y. Wang, J.X. Wang, H.Y. Li, S.B. Xi, C. Wei, P.X. Xi, G. E. Sterbinsky, J.W. Freeland, A.C. Fisher, J.W. Ager, Z.X. Feng, Z.J.C. Xu, Lattice site-dependent metal leaching in perovskites toward a honeycomb-like water oxidation catalyst, *Sci. Adv.* 7 (2021), eabk1788.
  - [31] E. Fabbri, M. Nachttegaal, T. Binninger, X. Cheng, B.J. Kim, J. Durst, F. Bozza, T. Graule, R. Schaublin, L. Wiles, M. Pertoso, N. Danilovic, K.E. Ayers, T. J. Schmidt, Dynamic surface self-reconstruction is the key of highly active perovskite nano-electrocatalysts for water splitting, *Nat. Mater.* 16 (2017) 925.
  - [32] B.W. Zhang, K. Jiang, H.T. Wang, S. Hu, Fluoride-induced dynamic surface self-reconstruction produces unexpectedly efficient oxygen-evolution catalyst, *Nano Lett.* 19 (2019) 530–537.
  - [33] J. Wang, S.J. Kim, J.P. Liu, Y. Gao, S. Choi, J. Han, H. Shin, S. Jo, J. Kim, F. Ciucci, H. Kim, Q.T. Li, W.L. Yang, K. Long, S.H. Yang, S.P. Cho, K.H. Chae, M.G. Kim, H. Kim, J. Lim, Redirecting dynamic surface restructuring of a layered transition metal oxide catalyst for superior water oxidation, *Nat. Catal.* 4 (2021) 212–222.
  - [34] M. You, L. Gui, X. Ma, Z. Wang, Y. Xu, J. Zhang, J. Sun, B. He, L. Zhao, Electronic tuning of  $\text{SrIrO}_3$  perovskite nanosheets by sulfur incorporation to induce highly efficient and long-lasting oxygen evolution in acidic media, *Appl. Catal. B Environ.* 298 (2021), 120562.
  - [35] X.B. Zhou, X.B. Liao, X.L. Pan, M.Y. Yan, L. He, P.J. Wu, Y. Zhao, W. Luo, L.Q. Mai, Unveiling the role of surface P-O group in P-doped  $\text{Co}_3\text{O}_4$  for electrocatalytic oxygen evolution by On-chip micro-device, *Nano Energy* 83 (2021), 105748.
  - [36] G. Wang, S.W. Jia, H.J. Gao, Y.W. Shui, J. Fan, Y.X. Zhao, L. Li, W.M. Kang, N. P. Deng, B.W. Cheng, The action mechanisms and structures designs of F-containing functional materials for high performance oxygen electrocatalysis, *J. Energy Chem.* 76 (2023) 377–397.
  - [37] P.Z. Chen, T.P. Zhou, S.B. Wang, N. Zhang, Y. Tong, H.X. Ju, W.S. Chu, C.Z. Wu, Y. Xie, Dynamic migration of surface fluorine anions on cobalt-based materials to achieve enhanced oxygen evolution catalysis, *Angew. Chem. Int. Ed.* 57 (2018) 15471–15475.
  - [38] Y. Kang, S. Wang, K.S. Hui, S.X. Wu, D.A. Dinh, X. Fan, F. Bin, F.M. Chen, J. X. Geng, W.C.M. Cheong, K.N. Hui, Surface reconstruction establishing Mott-Schottky heterojunction and built-in space-charging effect accelerating oxygen evolution reaction, *Nano Res.* 15 (2022) 2952–2960.
  - [39] Q.C. Xu, H. Jiang, X.Z. Duan, Z. Jiang, Y.J. Hu, S.W. Boettcher, W.Y. Zhang, S. J. Guo, C.Z. Li, Fluorination-enabled reconstruction of  $\text{NiFe}$  electrocatalysts for efficient water oxidation, *Nano Lett.* 21 (2021) 492–499.
  - [40] Y.N. Zhou, M.X. Li, S.Y. Dou, H.Y. Wang, B. Dong, H.J. Liu, H.Y. Zhao, F.L. Wang, J.F. Yu, Y.M. Chai, Promoting oxygen evolution by deep reconstruction via dynamic migration of fluorine anions, *ACS Appl. Mater. Interfaces* 13 (2021) 34438–34446.
  - [41] S. Anantharaj, S. Kundu, S. Noda, "The Fe Effect": a review unveiling the critical roles of Fe in enhancing OER activity of Ni and Co based catalysts, *Nano Energy* 80 (2021), 105514.
  - [42] Q.L. Han, Y.H. Luo, J.D. Li, X.H. Du, S.J. Sun, Y.J. Wang, G.H. Liu, Z.W. Chen, Efficient  $\text{NiFe}$ -based oxygen evolution electrocatalysts and origin of their distinct activity, *Appl. Catal. B Environ.* 304 (2022), 120937.
  - [43] C.F. Li, L.J. Xie, J.W. Zhao, L.F. Gu, H.B. Tang, L.R. Zheng, G.R. Li, Interfacial Fe-O-Ni-O-Fe bonding regulates the active Ni sites of Ni-MOFs via iron doping and decorating with  $\text{FeOOH}$  for super-efficient oxygen evolution, *Angew. Chem. Int. Ed.* 61 (2022), e202116934.
  - [44] X.T. Wang, T. Ouyang, L. Wang, J.H. Zhong, Z.Q. Liu, Surface reorganization on electrochemically-induced Zn-Ni-Co spinel oxides for enhanced oxygen electrocatalysis, *Angew. Chem. Int. Ed.* 59 (2020) 6492–6499.
  - [45] G. Kresse, J. Furthmüller, Efficiency of ab-initio total energy calculations for metals and semiconductors using a plane-wave basis set, *Comp. Mater. Sci.* 6 (1996) 15–50.
  - [46] G. Kresse, D. Joubert, From ultrasoft pseudopotentials to the projector augmented-wave method, *Phys. Rev. B* 59 (1999) 1758–1775.
  - [47] J.P. Perdew, J. Chevary, S. Vosko, K.A. Jackson, M.R. Pederson, D. Singh, C. Fiolhais, Atoms, molecules, solids, and surfaces: applications of the generalized gradient approximation for exchange and correlation, *Phys. Rev. B* 46 (1992) 6671–6687.
  - [48] J.P. Perdew, Y. Wang, Accurate and simple analytic representation of the electron-gas correlation energy, *Phys. Rev. B* 45 (1992) 13244.
  - [49] Y.L. Lee, M.J. Gadre, Y. Shao-Horn, D. Morgan, Ab initio GGA plus U study of oxygen evolution and oxygen reduction electrocatalysis on the (001) surfaces of lanthanum transition metal perovskites  $\text{LaBO}_3$  (B = Cr, Mn, Fe, Co and Ni), *Phys. Chem. Chem. Phys.* 17 (2015) 21643–21663.
  - [50] J.L. Liu, J.X. Xiao, Z.Y. Wang, H.M. Yuan, Z.G. Lu, B.C. Luo, E.K. Tian, G.I. N. Waterhouse, Structural and electronic engineering of Ir-doped Ni-(oxy) hydroxide nanosheets for enhanced oxygen evolution activity, *ACS Catal.* 11 (2021) 5386–5395.
  - [51] L.Q. Gui, Z.B. Wang, K. Zhang, B.B. He, Y.Z. Liu, W. Zhou, J.M. Xu, Q. Wang, L. Zhao, Oxygen vacancies-rich  $\text{Ce}_{0.9}\text{Gd}_{0.1}\text{O}_{2-\delta}$  decorated  $\text{Pr}_{0.5}\text{Ba}_{0.5}\text{CoO}_{3-\delta}$  bifunctional catalyst for efficient and long-lasting rechargeable Zn-air batteries, *Appl. Catal. B Environ.* 266 (2020), 118656.
  - [52] Y.C. Wei, Y. Zheng, Y. Hu, B.L. Huang, M.Z. Sun, P.F. Da, P.X. Xi, C.H. Yan, Controlling the cation exsolution of perovskite to customize heterostructure active site for oxygen evolution reaction, *ACS Appl. Mater. Interfaces* 14 (2022) 25638–25647.
  - [53] B. Bao, Y.N. Liu, M.Z. Sun, B.L. Huang, Y. Hu, P.F. Da, D.G. Ji, P.X. Xi, C.H. Yan, Boosting the electrocatalytic oxygen evolution of perovskite  $\text{LaCo}_{1-x}\text{Fe}_x\text{O}_3$  by the construction of yolk-shell nanostructures and electronic modulation, *Small* 18 (2022) 2201131.
  - [54] J.W. Zhao, H. Zhang, C.F. Li, X. Zhou, J.Q. Wu, F. Zeng, J.W. Zhang, G.R. Li, Key roles of surface Fe sites and Sr vacancies in the perovskite for an efficient oxygen evolution reaction via lattice oxygen oxidation, *Energy Environ. Sci.* 15 (2022) 3912–3922.
  - [55] Y.L. Zhu, W. Zhou, Y.J. Zhong, Y.F. Bu, X.Y. Chen, Q. Zhong, M.L. Liu, Z.P. Shao, A perovskite nanorod as bifunctional electrocatalyst for overall water splitting, *Adv. Energy Mater.* 7 (2017), 1602122.
  - [56] F. Gunkel, L. Jin, D.N. Mueller, C. Hausner, D.S. Bick, C.L. Jia, T. Schneller, I. Valov, R. Waser, R. Dittmann, Ordering and phase control in epitaxial double-perovskite catalysts for the oxygen evolution reaction, *ACS Catal.* 7 (2017) 7029–7037.
  - [57] H. Jo, Y.J. Yang, A. Seong, D. Jeong, J. Kim, S.H. Joo, Y.J. Kim, L.J. Zhang, Z. Liu, J.Q. Wang, S.K. Kwak, G. Kim, Promotion of the oxygen evolution reaction via the reconstructed active phase of perovskite oxide, *J. Mater. Chem. A* 10 (2022) 2271–2279.
  - [58] Y. Tong, J.C. Wu, P.Z. Chen, H.F. Liu, W.S. Chu, C.Z. Wu, Y. Xie, Vibronic superexchange in double perovskite electrocatalyst for efficient electrocatalytic oxygen evolution, *J. Am. Chem. Soc.* 140 (2018) 11165–11169.
  - [59] L. Trotochaud, S.L. Young, J.K. Ranney, S.W. Boettcher, Nickel-iron oxyhydroxide oxygen-evolution electrocatalysts: the role of intentional and incidental iron incorporation, *J. Am. Chem. Soc.* 136 (2014) 6744–6753.
  - [60] M. Gorlin, P. Chernev, J.F. de Araujo, T. Reier, S. Dresp, B. Paul, R. Krahnert, H. Dau, P. Strasser, Oxygen evolution reaction dynamics, faradaic charge efficiency, and the active metal redox states of Ni-Fe oxide water splitting electrocatalysts, *J. Am. Chem. Soc.* 138 (2016) 5603–5614.
  - [61] S. Hirai, S. Yagi, W.T. Chen, F.C. Chou, N. Okazaki, T. Ohno, H. Suzuki, T. Matsuda, Non-fermi liquids as highly active oxygen evolution reaction catalysts, *Adv. Sci.* 4 (2017), 1700176.
  - [62] J. Zhang, Y. Ye, Z.B. Wang, Y. Xu, L.Q. Gui, B.B. He, L. Zhao, Probing dynamic self-reconstruction on perovskite fluorides toward ultrafast oxygen evolution, *Adv. Sci.* 9 (2022), 2201916.
  - [63] L.J. Fan, E.L. Rautama, J. Linden, J. Sainio, H. Jiang, O. Sorsa, N.N. Han, C. Flox, Y. C. Zhao, Y.D. Li, T. Kallio, Two orders of magnitude enhancement in oxygen evolution reactivity of  $\text{La}_{0.7}\text{Sr}_{0.3}\text{Fe}_{1-x}\text{Ni}_x\text{O}_{3-\delta}$  by improving the electrical conductivity, *Nano Energy* 93 (2022), 106794.
  - [64] Y. Li, Y.Y. Wu, M.K. Yuan, H.R. Hao, Z. Lv, L.L. Xu, B. Wei, Operando spectroscopies unveil interfacial  $\text{FeOOH}$  induced highly reactive  $\beta\text{-Ni(Fe)OOH}$  for efficient oxygen evolution, *Appl. Catal. B Environ.* 318 (2022), 121825.
  - [65] Y. Li, Y.Y. Wu, H.R. Hao, M.K. Yuan, Z. Lv, L.L. Xu, B. Wei, In situ unraveling surface reconstruction of  $\text{Ni}_5\text{P}_4/\text{FeP}$  nanosheet array for superior alkaline oxygen evolution reaction, *Appl. Catal. B Environ.* 305 (2022), 121033.
  - [66] Y.Y. Wu, Y. Li, M.K. Yuan, H.R. Hao, X.J. San, Z. Lv, L.L. Xu, B. Wei, Operando capturing of surface self-reconstruction of  $\text{Ni}_3\text{S}_2/\text{FeNi}_2\text{S}_4$  hybrid nanosheet array for overall water splitting, *Chem. Eng. J.* 427 (2022), 131944.
  - [67] J.W. Zhao, Z.X. Shi, C.F. Li, Q. Ren, G.R. Li, Regulation of perovskite surface stability on the electrocatalysis of oxygen evolution reaction, *ACS Mater. Lett.* 3 (2021) 721–737.

- [68] X. Bo, R.K. Hocking, S. Zhou, Y.B. Li, X.J. Chen, J.C. Zhuang, Y. Du, C. Zhao, Capturing the active sites of multimetallic (oxy)hydroxides for the oxygen evolution reaction, *Energy Environ. Sci.* 13 (2020) 4225–4237.
- [69] M. Li, Y. Gu, Y.J. Chang, X.C. Gu, J.Q. Tian, X. Wu, L.G. Feng, Iron doped cobalt fluoride derived from CoFe layered double hydroxide for efficient oxygen evolution reaction, *Chem. Eng. J.* 425 (2021), 130686.
- [70] N.J. Hou, J.J. Gan, Q.S. Yan, Y.C. Zhao, Y.D. Li, Improved electrochemical oxidation kinetics of  $\text{La}_{0.5}\text{Ba}_{0.5}\text{FeO}_{3-\delta}$  anode for solid oxide fuel cells with fluorine doping, *J. Power Sources* 521 (2022), 230932.